Local atomic and electronic structure of the Pb/Si(111) mosaic phase: STM and *ab initio* study

Martin Švec,* Pavel Jelínek, Pavel Shukrynau, César González, and Vladimír Cháb
Institute of Physics, Academy of Science of the Czech Republic, Cukrovarnická 10, 162 53 Prague, Czech Republic

Václav Drchal
Institute of Physics, Academy of Science of the Czech Republic, Na Slovance 2, 182 21 Prague, Czech Republic
(Received 25 November 2007; revised manuscript received 6 February 2008; published 7 March 2008)

We have investigated the Pb/Si(111) mosaic phases of the surface with 1/6 monolayer Pb coverage at room temperature by means of scanning tunneling microscopy and spectroscopy and first-principles calculations. The dependence of the topographic height and electronic structure of Pb adatoms on the number of surrounding Si and Pb adatoms has been identified.

DOI: 10.1103/PhysRevB.77.125104 PACS number(s): 68.37.Ef, 71.15.Mb, 73.20.At

I. INTRODUCTION

Coverage of a Si(111)-7×7 surface with lead atoms of up to one monolayer (ML) produces two distinct phases of $(\sqrt{3}\times\sqrt{3})R30°$ symmetry.[1–3] The first, known as the β phase, is obtained around coverages of 1/3 ML. It is formed by a complete overlayer of Pb atoms at T_4 positions and usually coexists with islands of the 1×1 phase with 1 ML of Pb coverage.[4,5] The second phase is a mixture of 50% of Pb adatoms and 50% of Si adatoms in the topmost layer, with total Pb coverage of 1/6 ML. The chainlike arrangement of Pb and Si atoms in the $(\sqrt{3}\times\sqrt{3})R30°$ lattice is called the *mosaic* phase.[6,7] In all these phases, the bonding configuration of Pb and Si is very similar: Each adatom is located on a T_4 position over the Si(111) surface with four valence electrons in an sp^3-like hybridization and one dangling bond pointing outward from the surface plane. In spite of this relatively simple structure, the surface electronic structure is rather complicated and differs from one phase to another due to electronic correlations between the Pb and Si adatoms. The chemical disorder of the surface prevents determination of an elementary periodic cell. In a hypothetically ideal case, where the entire layer is formed by alternating Pb and Si chains, each atom would have two chemically identical and four other-species neighbors and a $(2\sqrt{3}\times 2\sqrt{3})R30°$ periodic cell could be defined. Previous experimental and theoretical[8] investigations indicate that while the pure phase shows a metallic behavior, the mosaic phase displays a semiconductor tendency toward charge-transfer effect from the Si to the Pb adatoms. Comparable structures were observed also in isoelectronic systems, namely, 1/6 ML Sn/Si(111) (Refs. 9–12) and (Pb,Sn)/Ge(111).[13] The Pb/Si(111) mosaic phase is very stable—after formation, it does not undergo any phase transition in the range between 0 K and the temperature of Pb desorption.[14] Recently, the mosaic phase has been used to demonstrate the single atom chemical identification using atomic force microscopy.[15]

However, the real mosaic shows more complicated electronic and structural properties. Experimental scanning tunneling microscopy (STM) study combined with the Monte Carlo simulations suggested a practical realization of the two-dimensional (2D) Ising system,[16] but the character and range of interatomic interaction are left unknown. Large distances between nearest neighbor adatoms on the surface exclude their direct chemical interactions and it seems that there is no substantial charge transfer among Si and Pb atoms. Our previous studies of the β phase demonstrate the possibility of intra-atomic charge redistribution and the effect of the shallow core levels on the Si-Pb bonding.[17,18] Thus, a complex interaction as interplay between the energy of elastic deformation, band energy, and intra-atomic charge redistribution might play an important role in the formation and stabilization of both phases.

Based on these assumptions, local electronic properties of the mosaic phase, namely, local density of states (LDOS) connected with particular atoms in chains, may be crucial in determining the character of the charge redistribution and may lead to an explanation of the growth process and mechanism responsible for ordering. In particular, the real-space map of LDOS taken with atomic resolution would be very important.

Here, we report the experimental and theoretical study of the Pb $(\sqrt{3}\times\sqrt{3})R30°$ phase on the Si(111) surface. In particular, we draw our attention to relation between structural and electronic properties of the mosaic phase. As the mosaic phase is chemically disordered, reciprocal-space methods cannot be used to identify orbitals participating in bonding at the metal/semiconductor interface. A combination of STM and scanning tunneling spectroscopy (STS) measurements with density functional theory (DFT) calculations has been applied to investigate the dependence of LDOS on a local atomic configuration as a function of the chemical nature of its neighbors. Special attention was concentrated on the intra-atomic charge redistribution resulting in the local metal or semiconductor character of this 2D alloy.

II. EXPERIMENTAL AND THEORETICAL METHODS

The sample was cut from a *p*-doped Si(111) wafer with a resistivity of 1–10 $\Omega\,\mathrm{cm}^{-1}$ and degassed overnight at 600 °C. A clean Si(111)-7×7 surface was obtained by flashing the *p*-doped sample several times to 1200 °C followed by slow cooling from 850 °C to room temperature at a rate of approximately 30 °C/min.[14] Lead was evaporated from a water-cooled electron-beam source (EFM3, Focus, Omicron Ltd.) with an ion flux of 100 nA for 10 min. An-

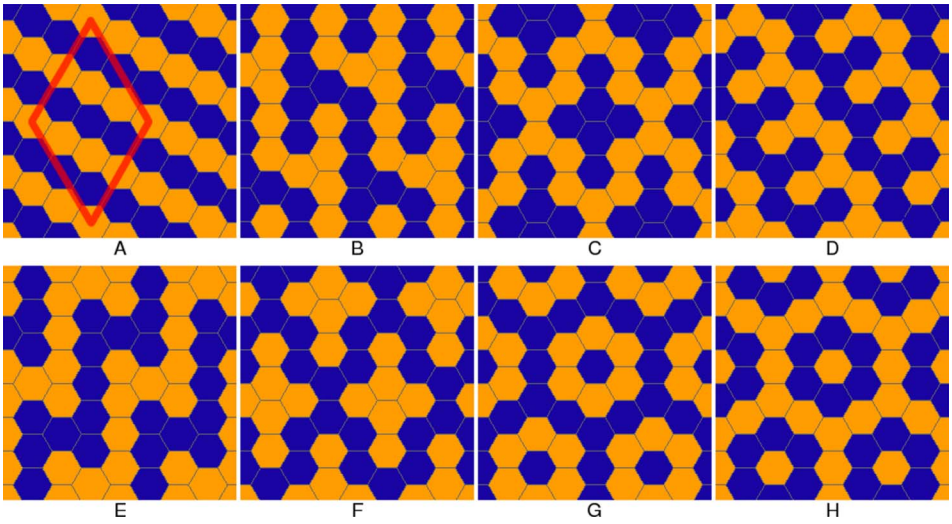

FIG. 1. (Color online) Schematic view of eight atomic structures of mosaic phase used for calculations. Yellow (light gray) hexagons present silicon atoms and blue (dark gray) lead atoms. A common elementary (6×6) cell is drawn in (A).

nealing for few minutes to 800 °C caused a rapid decrease in Pb content until the coverage of 1/6 ML was achieved.[1]

The STM used was a commercial UHV variable-temperature Omicron instrument with a base pressure of 1×10^{-10} mbar and a maximum pressure during evaporation of 5×10^{-10} mbar. First, we measured standard topography for reference. Afterward, current and dI/dV (lock-in) maps were taken simultaneously. Details of the technique are described elsewhere.[19] For STS at single points, we used a lock-in amplifier in the same setup as for the dI/dV maps. The tunneling distance was held constant and voltage was ramped from −1.5 to 1.5 V, while current and dI/dV signal were recorded. The dI/dV curves were verified by comparison with a digital derivation of the current. Determination of the band gap widths and valence band (VB) edge positions is, however, not possible from simple dI/dV due to the strong attenuation of the spectra around zero voltage (Fermi level), which is usual for ultrathin metallic layers on semiconductor substrates. To overcome this problem, we used the *I-V* curves to evaluate the VB edge correctly.

Understanding the relationship between the electronic structure and local atomic arrangement of the mosaic phase is not an easy task due to the complicated nonperiodic atomic structure. Addressing this complex problem with a fully converged first-principles description in terms of an extended orbital basis such as plane waves would limit our calculations (due to the computational resources needed) to a simple geometry, while a set of atomic configurations, within a supercell approach, is needed in order to provide a reliable comparison between the calculated structures and the experimental data. An appropriate choice, which we follow in this paper, is to resort to local orbital DFT methods, especially those derived with the aim of computational efficiency such as the FIREBALL code.[20–23] This method offers a very favorable accuracy and/or efficiency balance if the atomiclike basis set[24] is chosen carefully.

The valence wave functions are expanded in the FIREBALL orbitals,[20] a set of strictly localized pseudoatomic orbitals [exactly equal to zero for distances larger than the cutoff radius (R_C)]. In particular, we have used a basis that includes *s*, *p* and *d* orbitals for both Si and Pb elements. In the case of Pb, based on previous experience with transferability of pseudopotentials,[7,25] we used a pseudopotential involving semicore 5*d* electron states in the VB. In our calculation, we adopted the following cutoff radii: R_C (Si *s* orbital) =4.8 a.u., R_C (Si *p* orbital)=5.4 a.u., and R_C (Si *d* orbital) =5.2 a.u. and R_C (Pb *s*,*p*, and *d* orbitals)=5.5 a.u. This basis set yields a very good description of both the bulk and surface properties: In the case of Si, we have obtained for the bulk diamond structure a lattice parameter $A=5.46$ Å and a bulk modulus $B=105$ GPa (experiment: $A=5.43$ Å and $B=100$ GPa), while for 1/3 ML of Pb on Si(111), we have found a 3×3 reconstruction with two Pb atoms down and one up as the ground state structure, in good agreement with the experimental evidence.[7]

In our simulations, we use a supercell approach considering eight different atomic models of the Pb/Si(111) mosaic phase (see Fig. 1). The surface alloy layer contained six Si and Pb atoms, respectively, keeping a proper 1:1 ratio between species in the mosaic phase. The structures were selected so as to mimic frequently observed local atomic patterns acquired from a previous STM analysis. In our calculations, we have chosen a supercell with (6×6) periodicity that naturally accommodates the $(\sqrt{3}\times\sqrt{3})R30°$ surface reconstruction. The slab was formed by six Si layers and hydrogen atoms saturating the bonds of the deeper Si layer. The last two layers of the slab, the deeper Si and passivated H layer, were kept fixed during the relaxation process. Our supercell contains, in total, 248 atoms. Two *k* points were included in the sampling of the Brillouin zone. Each atomic configuration was allowed to relax to its ground state configuration, with convergence criteria for the total energy and forces of 10^{-6} eV and 0.05 eV/Å.

Theoretical STM images of optimized surfaces were calculated using the combination of the optimized DFT local-orbital Hamiltonian and Keldysh–Green-function formalism.[26,27] We used a tungsten tip consisting of five atoms having a pyramidal structure. A more detailed description of the computational method can be found elsewhere.[27–29]

In addition, we have adopted the cluster expansion technique[30] combined with first-principles total energy calcu-

lations to unveil the character of the adatom-adatom interaction between different species in the Pb/Si(111) mosaic phase. The total energy of a binary alloy A_xB_{1-x} (in our case A equals the Pb and B the Si adatom) can be expressed in terms of cluster expansion,

$$E = \sum_n v_n \xi_n, \tag{1}$$

where v_n are cluster interaction potentials and ξ_n are multisite correlation functions defined on nth order cluster. The sum runs over all cluster types. The correlation function is defined as

$$\xi_n = \frac{1}{N_n} \sum_{\{p_i\}} \sigma_{p_1} \sigma_{p_2} \cdots \sigma_{p_n}, \tag{2}$$

where $\sigma_p = 1$ if the lattice point p is occupied by the atom A (Pb adatom), and $\sigma_p = -1$ if it is occupied by atom B (Si). The sum is over all clusters of type n on the lattice; the total number of such clusters is N_n.

The interaction cluster potentials are obtained through the inversion of Eq. (1),

$$v_n = \sum_m E_m (\xi_{n,m})^{-1}, \tag{3}$$

where m enumerates the structures of Table I.

Some of the correlation functions [Eq. (2)] may be linearly dependent on the others because we use a finite elementary cell and a fixed chemical composition of clusters (six Pb and six Si atoms). The dependent clusters can be detected using the singular value decomposition[31] and then excluded from the analysis.

III. RESULTS AND DISCUSSION

A. Scanning tunneling microscopy experiment

Figure 2 shows characteristic STM images of the mosaic phase using both constant current and constant height operation mode. We can clearly distinguish two kinds of protrusions by the contrast difference in the STM images. Since the distances between them coincide with the geometry expected for the adatoms of the $\sqrt{3}$ structure, we have labeled them as bright and dim adatoms. An estimation of their proportion can be derived from large images typically containing over a thousand adatoms by counting both adatom types. In the images of the mosaic phase, we have found mostly one-half of bright adatoms and a one-half of dim adatoms. When imaging this surface with STM, a different topographic behavior is observed in both polarities. In filled-state images, Si adatoms appear as a hole and Pb adatoms as bright spots. In empty-state images, the Si adatoms are generally visible with slightly dimmer contrast, and the Pb adatom appearance does not differ too much from that of Si adatoms at the surface. Here, we should note that STM images are driven by electronic effects that dominate over structural differences and the images map the LDOS of the surface.

From a direct comparison between the constant current and the constant height STM images (see Fig. 2), it is evident that the constant height images [see Figs. 2(c) and 2(d)] yield

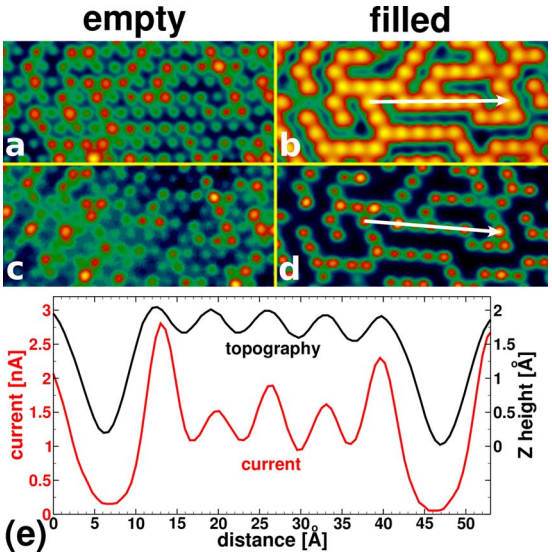

FIG. 2. (Color online) Standard topography taken at bias (a) 1.5 V and (b) −1.5 V at a feedback current of 0.56 nA and constant-height current images taken at (c) 1.5 V and (d) −1.5 V from the same area. (e) Line profiles over a row of Pb atoms for the topography and the current filled-state images; white arrows in the filled-state images show the location of the profiles.

an enhancement of the image contrast. The *current images* reveal a fine difference between the electronic properties of individual Pb adatoms according to their local chemical environment. This can be clearly seen from profiles of the same Pb row drawn for both methods [Fig. 2(e)]. In a careful inspection of the current images of these surfaces, Pb adatoms with different contrasts have been identified, especially at places where chains of Pb adatoms cross and split. The variation of the image contrast can also be found between different polarities. In particular, protrusion of the Pb adatoms in filled-state images $(-0.5\ldots,-1.5$ eV) is generally reduced with increasing number of the nearest neighbors of the same species (NNSS). In contrast, the empty-state STM images $(+0.5,\ldots,+1.5$ V) display Pb adatoms with a higher NNSS brighter than the rest of the Pb and Si atoms. Based on these experimental observations, we can conclude that the electronic and geometrical configurations of adatoms is mostly driven by the composition of the nearest neighbors. To provide a more quantitative analysis of the effect, we have performed an extensive study to reveal the relation between the local arrangement around Pb atoms and their contrast in the STM images.

The position of individual adatoms in the Pb/Si(111) mosaic phase can be mapped onto a triangular lattice. Each site is surrounded with six nearest neighbor sites, where an individual site can be occupied by an Si or Pb adatom, respectively. Considering all possible arrangements of the nearest neighbor sites surrounding the central site occupied by an Pb adatom, a total of 13 different arrangements are possible. These patterns are mutually independent in such a way that no combination of mirror and rotation operations can transform one of these motives into another. These motives can be further sorted into seven categories, depending on the total

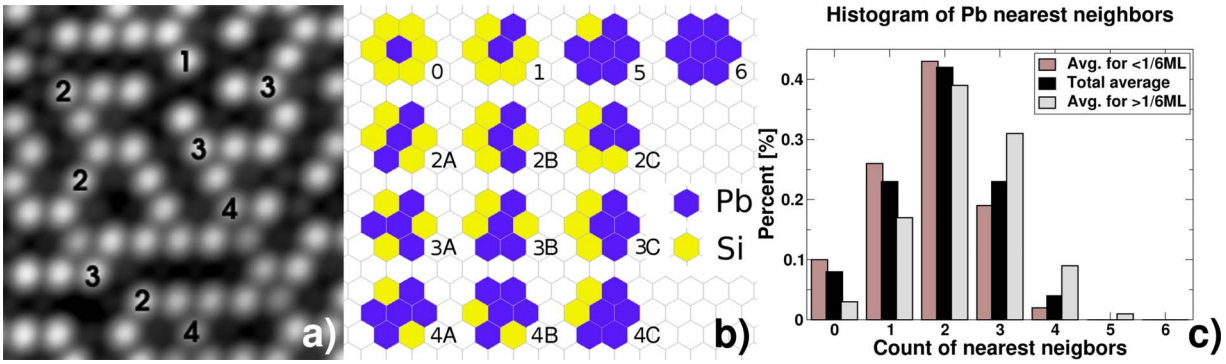

FIG. 3. (Color online) (a): an example of attributing the number of NNSS to the atoms in the topography, (b): 13 independent possible arrangements of Pb and Si adatoms around a Pb atom, and (c): a histogram obtained by analysis of ten 100×100 nm^2 images.

number of their Pb nearest neighbors [for an example of attributing numbers, see Fig. 3(a)]. Figure 3(b) shows all possible configurations that we have taken into account in our analysis. We have labeled the individual configurations in the following manner: The numbers 0–6, denoting the number of the Pb NNSS, are attributed to individual arrangements of NNSS and we add letters (3A, 3B, etc.) to distinguish between degenerate cases of the NNSS arrangement.

A distribution analysis of the NNSS performed by counting the Pb and Si adatoms and their NNSS in ten STM images (scanning area of 100×100 nm^2) produced a histogram [Fig. 3(c)]. We have found configurations with two NNSS to be the most frequent, but configurations with one and three NNSSs are represented in significant amounts as well. The clusters have no long-range order among the observed regions.

To obtain more information about the local electronic structure of the mosaic phase, we have performed the lock-in measurements of the mosaic phase at different bias voltages. An illustration of the lock-in (dI/dV) mapping results is shown in Fig. 4 for selected energies over a representative region of 5×5 nm^2. One can see a typical contrast variation of the Pb atom within configurations 1–5 (see labeled spots in Fig. 4). Beginning at −0.3 eV below the Fermi level, all Pb adatoms except chain end atoms (configuration 1) show equal contrast. At −0.5 eV, the end atoms become more apparent whereas most Pb atoms with configurations 3–5 become dimmer. End-atom intensity culminates at around −0.9 eV, while the Pb adatoms with three to five NNSS are the weakest. At −1.5 eV, the appearance of the dI/dV map is similar to the −0.5 eV one. Consistent with the current images, only a small contrast of Si adatoms in the filled states images is observed. On the other hand, the empty states lock-in images obtained up to 1 eV show small differences between Pb and Si adatoms. Only Pb adatoms having configurations 4 and 5 emerge strongly at 0.3 eV. At voltages above 1.2 eV, all of the Pb adatoms appear to be dominant analogously to the filled states.

To compare directly the electronic properties of individual Pb adatoms, we carried out an additional STS measurement. Characteristic dI/dV curves for a Pb adatom with configurations 1–4 are presented in Fig. 5. The plot reveals a strong correlation between the number of NNSS and the position of the highest electronic state below the Fermi level. Namely, an increasing number of NNSS of the Pb adatom shifts the peak in filled states toward the Fermi level. A similar measurement carried out at the β phase did not reveal any similar effects.

The separations of the VB edge from the Fermi level for a set of 20 Pb atoms with different NNSS are plotted in Fig. 6. Pb atoms with 0, 1, and 2 NNSS have the edge clearly separated from the Fermi level, whereas for Pb atoms with four,

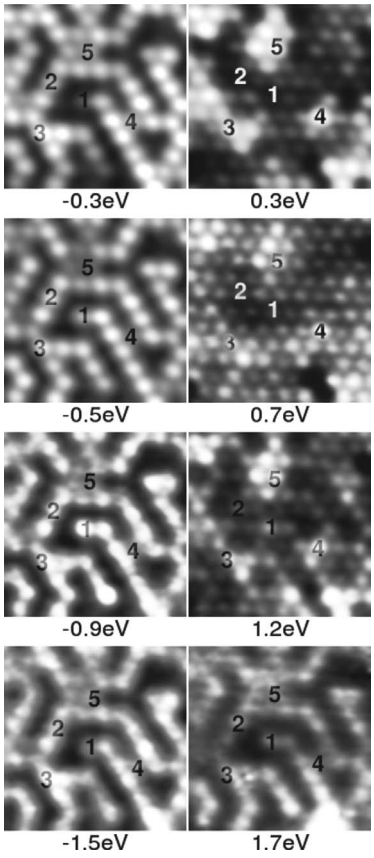

FIG. 4. Lock-in dI/dV maps of an area of 5×5 nm^2, filled (left column) and empty (right column) states. Representative atoms with one to five NNSS are marked with numbers.

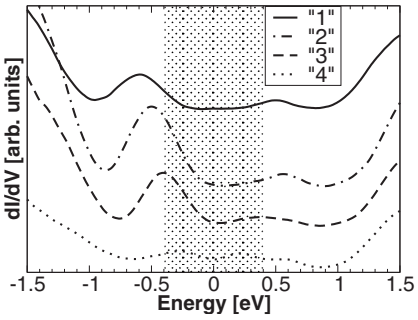

FIG. 5. Typical dI/dV curves for Pb adatoms with one to four NNSS. A strong correlation between the peak position and the number of neighbors is observed.

five, and six NNSS, the VB edge reaches the Fermi level, as well as for some with 3 NNSS.

B. Theoretical calculations

We performed total energy calculations for eight selected patterns of the Pb/Si(111) mosaic phase within a (6×6) unit cell, as schematically shown in Fig. 1. Table I presents the comparison of total energies between the considered structures. We have found that ideal structure *A* has the minimum total energy among the studied patterns. The ideal structure is formed by infinite one-dimensional (1D) atomic chains and has a semiconductor character with a gap of ≈0.9 eV. The vertical displacement between Pb and Si adatoms in the surface layer is 0.96 Å. The electronic and structural configurations of Pb adatoms are practically identical to *up* Pb adatoms of the Pb/Si(111)-(3×3) phase, having almost identical bond lengths and angles (listed in Table II) in $PbSi_4$ surface tetrahedra (see Fig. 7) and the position of a density of states (DOS) peak of semicore 5*d* Pb electrons. In this ideal case, each Pb adatom has two Pb and four Si nearest neighbor atoms.

We also performed an analysis of the electronic structure and vertical displacement of adatoms of the rest of the fully relaxed atomic patterns (B)–(H) of the mosaic phase (see Fig. 1). We found a direct dependence of both the structural and electronic properties of adatoms on the local atomic arrangement. Namely, the position of the highest occupied and unoccupied bands varies significantly according to the type of nearest neighbor adatoms, Si or Pb, respectively. The vertical displacement of Si adatoms does not show marked sensitivity to the local chemical composition varying around ≈0.02 Å. On the other hand, Pb adatoms embody more pronounced vertical displacement, ≈0.1 Å. From the inset of Fig. 6, it is evident that high and low numbers of nearest neighbor Pb adatoms pushes the Pb adatoms downward and upward, respectively. However, the dispersion of the vertical displacement of adatoms for the given number of the NNSS indicates that the adatom-adatom interactions go beyond the nearest neighbor pairs, in good agreement with experimental evidence.

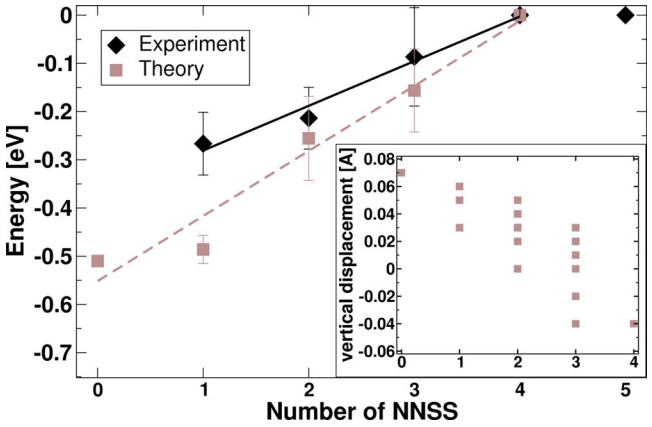

FIG. 6. (Color online) Theoretical and experimental values of VB separation from Fermi level for Pb adatoms as a function of NNSS.

TABLE I. Table contains list of configurations studied here together with the list of the sites occupied by Pb adatoms and their total energies calculated from the DFT. Individual sites are denoted according to Fig. 8.

Label	Occupied sites	E_{tot} (eV)
A	1, 4, 5, 8, 10, 11	−0.81
B	4, 5, 7, 9, 10, 11	−0.55
C	1, 5, 6, 7, 8, 12	−0.41
D	1, 2, 3, 4, 9, 10	−0.65
E	2, 4, 5, 8, 9, 11	−0.23
F	2, 3, 4, 9, 10, 11	−0.46
G	2, 7, 9, 10, 11, 12	−0.70
H	1, 3, 4, 5, 6, 8	−0.68

According to Löwdin charge analysis, we found a significant charge transfer of ≈0.3 electron from Pb adatoms to underneath Si atoms (see atoms Si_1 and Si_3 in Fig. 7). The atomic Löwdin charges of individual atoms remain practically constant under different atomic configurations we have considered. On the other hand, we have found a significant rearrangement of the charge in the dangling bond according to the local chemical configuration. In general, the upward displacement of Pb adatoms (Fig. 6) is associated with the

TABLE II. Comparison of bond lengths and angles for nearest neighbor atoms surrounding a Pb adatom. The two states of Pb adatom are labeled up and down in the Pb/Si(111)-(3×3) phase and in an ideal structure of mosaic phase forming infinite 1D chains [see Fig. 1(a)]. These are numbered according to Fig. 7.

Bond	Down (3×3)	Up (3×3)	Mosaic
Pb-Si_1	2.78 Å	2.80 Å	2.80 Å
Si_1-Si_2	3.67 Å	3.47 Å	3.45 Å
Si_2-Si_3	2.38 Å	2.37 Å	2.36 Å
Pb-Si_3	2.89 Å	3.23 Å	3.26 Å
Si_3-Si_4	2.38 Å	2.31 Å	2.31 Å
∠Pb-Si_1-Si_3	67.4°	76.8°	77.9°

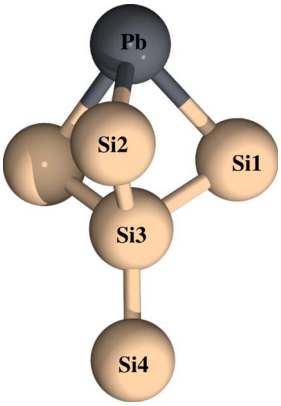

FIG. 7. (Color online) Schematic view of characteristic atomic arrangement of Pb adatoms and four Si atoms underneath in the Pb/Si(111) mosaic phase.

shift to lower energies of their corresponding dangling bond. Note that the same effect has been observed on a Sn/Si(111) surface with Si defects.[11]

Calculated occupied states STM images of fully relaxed structures (E and F) show Pb adatoms as bright spots and Si adatoms as practically invisible, in good agreement with experimental observations (see Fig. 9). The atomic STM contrast of Pb adatoms slightly changes according to the local pattern. We can observe a general tendency that the increasing number of NNSS adatoms around the Pb adatom induces a depression in STM filled-state images. This effect can be simply explained by the vertical relaxation of Pb adatoms driven by the number of NNSS adatoms because an increased number of Pb adatoms leads to a downward relaxation of the central Pb adatom (see the inset of Fig. 6) together with the redistribution of the electron charge localized on the dangling bond (see Fig. 10).

To understand the character of the adatom-adatom interaction between different species in the mosaic phase, we have adopted the cluster expansion technique[30] combined with first-principles total energy calculations. In our analysis, we have used the eight different configurations within a (6 $\times$6) unit cell (see Table I) introduced above. The cluster

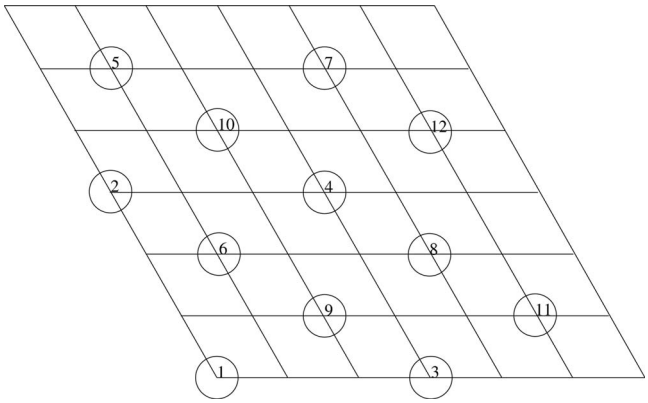

FIG. 8. Schematic view of (6$\times$6) elemental cell used in the cluster expansion with numbering of sites.

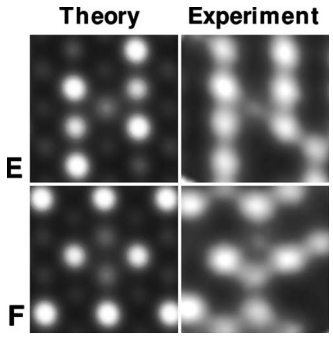

FIG. 9. Comparison of experimental simulated current maps for patterns E and F (cf. Fig. 1).

expansion was formulated using the 11 independent elemental clusters listed in Table III.

The effective cluster interactions v_n obtained from the cluster expansion analysis are listed in Table IV. A rapid decrease in the effective interaction parameters v_n for higher clusters indicates a good convergence of the cluster expansion. We have found a dominant contribution of the nearest neighbor effective interactions, which have ordering character.

The linear dependence of the single site term results from the fact that we have considered only configurations with a constant concentration of Pb and Si adatoms. On the other hand, the linear dependence of the third neighbor pair and the linear triangle is a consequence of the rather small (6 $\times$6) unit cell used here.

C. Discussion

Both the experimental and theoretical results point to the strong variation of electronic structure according to local

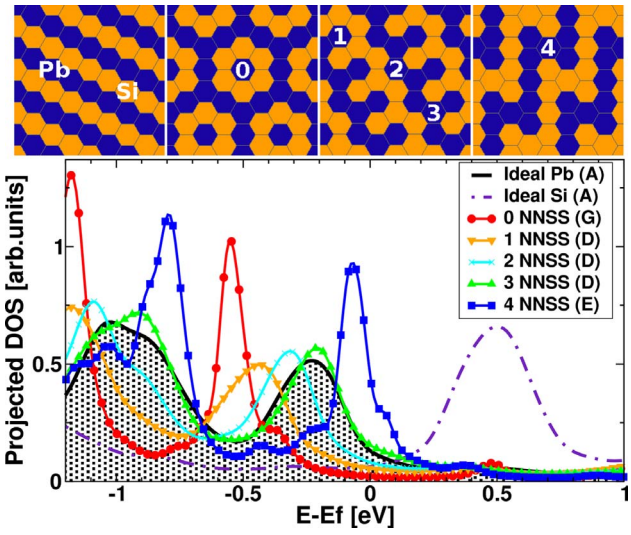

FIG. 10. (Color online) The figure shows the calculated projected DOS of a selected Pb adatom with different local atomic configurations. The schematic view of the individual adatoms and their configuration is provided in the upper part of the figure. The Fermi level is set to zero.

TABLE III. Clusters considered within the (6×6) unit cell. Here, m means multiplicity and v is the number of vertices; the last column contains the hexagonal coordinates of vertices.

n	Cluster	m	v	Vertices
1	Absolute term	1	0	∅
2	Single site	12	1	(0,0)
3	Nearest neighbors	36	2	(0,0), (2,1)
4	Second neighbors	36	2	(0,0), (3,0)
5	Third neighbors	36	2	(0,0), (4,2)
6	Equilateral triangle	24	3	(0,0), (2,1), (1,2)
7	Linear triangle	36	3	(0,0), (2,1), (4,2)
8	Isosceles triangle	72	3	(0,0), (2,1), (3,0)
9	Rectangular triangle	144	3	(0,0), (3,0), (4,2)
10	Quadrangle	36	4	(0,0), (2,1), (3,3), (1,2)
11	Hexagon	12	6	Six nearest neighbors of (0,0)

chemical composition from semiconductor to metallic character (from semiconductor to metallic character). Figure 6 compares averaged experimental and theoretical values of VB separation from the Fermi level as a function of the NNSS. Both experimental and theoretical values grow almost linearly with the number of NNSS. Theoretical prediction follows a slightly steeper trend than experiment. Both curves match for adatoms with four NNSS near the Fermi level. Further increasing the NNSS induces a further shift of the VB above the Fermi level. In contrast, for adatoms with zero, one, and two NNSS, the separation is more than 0.2 eV, thus a local gap opens and the adatoms behave as semiconducting adatoms.

The DFT simulations of the mosaic reproduce the shift direction and magnitude of the LDOS peaks, in good agreement with experiment. However, the positions of peaks do not fit exactly. This can be explained by possible distortions of STS spectra caused by local analogs of band-bending effects.

A detailed analysis of the band gap shift unveils a complex correlation with the local adatom composition, going beyond the nearest neighbor adatom, as is evident from the error bar width in Fig. 6. In particular, let us consider two similar Pb adatom configurations having the same number of first, second, and third nearest neighbors (Fig. 11) (we neglect the influence of further neighbors because of their distance). The LDOS peaks are mutually shifted by ≈0.2 eV.

TABLE IV. Effective cluster interactions v_n obtained from the cluster expansion analysis.

n	Cluster	v_n (eV)	Note
1	Absolute term	0.0075	
2	Single site	0.0	Linear dependence
3	Nearest neighbors	2.2275	
4	Second neighbors	0.1575	
5	Third neighbors	0.0	Linear dependence
6	Equilateral triangle	0.0150	
7	Linear triangle	0.0	Linear dependence
8	Isosceles triangle	0.7200	
9	Rectangular triangle	0.0900	
10	Quadrangle	−0.0225	
11	Hexagon	0.0000	

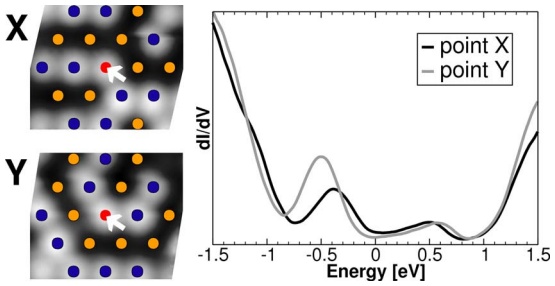

FIG. 11. (Color online) STS measured at two Pb adatoms with the same number of first, second, and third nearest neighbors, but with a different distribution, demonstrating the influence on the dI/dV curve.

The performed experimental and theoretical analysis point out that the dispersion of the LDOS is driven mainly by the arrangement of the first nearest atoms, but distribution of the second and third nearest atoms and their mutual configurations also matters. To work out any unique conclusions in this sense, one would need to collect and analyze a considerably bigger dataset than has been done in this work.

IV. CONCLUSIONS

In conclusion, we have performed an analysis of the local character of the atomic and electronic structures of the mosaic phase using a combination of the STM experiment and the fully relaxed *ab initio* DFT calculations. We have found that electronic structure varies locally according to the chemical composition of surrounding adatoms. With an increasing number of nearest neighbor Pb atoms, the Pb LDOS peaks in occupied states are strongly shifted toward the Fermi level and the character of such Pb atoms changes from semiconducting to metallic. From the performed analysis, it is evident that the correlations between the position of the VB and the local chemical composition goes beyond the nearest neighbor adatoms. In our cluster expansion analysis, we found the dominant nearest neighbor effective repulsive interaction of ordering type acting between the same species. Furthermore, DFT calculations showed that the energetically most favored structure among the considered models consists of alternating Pb and Si 1D infinite chains with a semiconductor character. It remains unclear why the mosaic phase has the disordered character.

ACKNOWLEDGMENTS

This work was supported from Grants No. IAA1010413, No. AVOZ10100520, No. AV0Z10100521, KAN400100701, and No. IAA100100616. C.G. gratefully acknowledges the financial support from MEC in Spain under Grant No. 2007-0034.

*svec@fzu.cz

[1] E. Ganz, I.-S. Hwang, F. Xiong, S. K. Theiss, and J. Golovchenko, Surf. Sci. **257**, 256 (1991).
[2] G. LeLay, J. Peretti, and M. Hanbücken, Surf. Sci. **204**, 57 (1988).
[3] P. J. Estrup and J. Morrison, Surf. Sci. **2**, 465 (1964).
[4] H. H. Weitering, A. R. H. F. Ettema, and T. Hibma, Phys. Rev. B **45**, 9126 (1992).
[5] J. Slezák, P. Mutombo, and V. Cháb, Phys. Rev. B **60**, 13328 (1999).
[6] J. M. Gómez-Rodríguez, J.-Y. Veuillen, and R. C. Cinti, J. Vac. Sci. Technol. B **14**, 1005 (1996).
[7] I. Brihuega, O. Custance, R. Pérez, and J. M. Gómez-Rodríguez, Phys. Rev. Lett. **94**, 046101 (2005).
[8] T.-L. Chan, C. Z. Wang, M. Hupalo, M. C. Tringides, Z.-Y. Lu, and K. M. Ho, Phys. Rev. B **68**, 045410 (2003).
[9] Y. Sugimoto, O. Custance, S. Morita, M. Abe, P. Pou, P. Jelínek, and R. Pérez, Phys. Rev. B **73**, 205329 (2006).
[10] Y. Sugimoto, M. Abe, K. Yoshimoto, O. Custance, I. Yi, and S. Morita, Appl. Surf. Sci. **241**, 23 (2005).
[11] W. Kaminski, P. Jelínek, R. Pérez, F. Flores, and J. Ortega, Appl. Surf. Sci. **234**, 286 (2004).
[12] B. Ressel, C. D. Teodoro, G. Profetta, L. Ottaviano, V. Cháb, and V. Prince, Surf. Sci. **562**, 128 (2004).
[13] A. Charrier, R. Pérez, F. Thibaudau, J.-M. Debever, J. Ortega, F. Flores, and J.-M. Themlin, Phys. Rev. B **64**, 115407 (2001).
[14] B. Ressel, J. Slezák, K. C. Prince, and V. Cháb, Phys. Rev. B **66**, 035325 (2002).
[15] Y. Sugimoto, P. Pou, M. Abe, P. Jelínek, R. Pérez, S. Morita, and O. Custance, Nature (London) **446**, 64 (2007).
[16] L. Ottaviano, B. Ressel, C. Di Teodoro, G. Profeta, S. Santucci, V. Cháb, and K. C. Prince, Phys. Rev. B **67**, 045401 (2003).
[17] M. Švec, V. Dudr, M. Vondráček, P. Jelínek, F. Šutara, V. Matolín, K. C. Prince, and V. Cháb (unpublished). prepared for submission.
[18] V. Dudr, N. Tsud, S. Fabík, M. Vondráček, V. Matolín, V. Cháb, and K. C. Prince, Phys. Rev. B **70**, 155334 (2004).
[19] M. Švec, P. Mutombo, P. Shukrynau, V. Dudr, and V. Cháb, Nanotechnology **17**, 213 (2006).
[20] O. F. Sankey, D. J. Niklewski, D. A. Drabold, and J. D. Dow, Phys. Rev. B **41**, 12750 (1990).
[21] A. A. Demkov, J. Ortega, O. F. Sankey, and M. P. Grumbach, Phys. Rev. B **52**, 1618 (1995).
[22] J. P. Lewis, K. R. Glaesemann, G. A. Voth, J. Fritsch, A. A. Demkov, J. Ortega, and O. F. Sankey, Phys. Rev. B **64**, 195103 (2001).
[23] P. Jelínek, H. Wang, J. P. Lewis, O. F. Sankey, and J. Ortega, Phys. Rev. B **71**, 235101 (2005).
[24] M. A. Basanta, Y. J. Dappe, P. Jelinek, and J. Ortega, Comput. Mater. Sci. **39**, 759 (2007).
[25] S. Brochard, E. Artacho, O. Custance, I. Brihuega, A. M. Baró, J. M. Soler, and J. M. Gómez-Rodríguez, Phys. Rev. B **66**, 205403 (2002).
[26] N. Mingo, L. Jurczyszyn, F. J. García-Vidal, R. Saiz-Pardo, P. L. de Andres, F. Flores, S. Y. Wu, and W. More, Phys. Rev. B **54**, 2225 (1996).
[27] J. M. Blanco, F. Flores, and R. Pérez, Prog. Surf. Sci. **81**, 403 (2006).
[28] J. M. Blanco, C. González, P. Jelínek, J. Ortega, F. Flores, and R. Pérez, Phys. Rev. B **70**, 085405 (2004).
[29] J. Blanco *et al.*, Phys. Rev. B **71**, 113402 (2005).
[30] J. W. D. Connolly and A. R. Williams, Phys. Rev. B **27**, 5169 (1983).
[31] W. H. Press, S. A. Teukolsky, W. T. Vetterling, and B. P. Flannery, *Numerical Recipes in Fortran* (Cambridge University Press, Cambridge, 1992).